Emergence of bistability and even-order harmonic generation in a centrosymmetric system under periodic driving

Fumiya Sekiguchi,[1,*] Yuta Murotani,[2] and Ryo Shimano[1,3,†]

[1] *Cryogenic Research Center, The University of Tokyo, Yayoi, Tokyo 113-0032, Japan*

[2] *The Institute for Solid State Physics, The University of Tokyo, Kashiwa, Chiba 277-8581, Japan*

[3] *Department of Physics, The University of Tokyo, Hongo, Tokyo 113-0033, Japan*

(Received 12 December 2025; revised 14 March 2026; accepted 9 June 2026; published 10 July 2026)

Nonequilibrium states of matter, when driven periodically, can exhibit exotic properties and emergent behaviors that are fundamentally distinct from those in equilibrium systems. To investigate the dynamical behavior of a particle system under time-periodic external forces, we performed numerical simulations of the motion of a particle initially trapped in an inverted Gaussian potential. Under strong driving, the center of motion of the particle shifts away from the origin of the trap potential, either toward the positive or negative direction. This behavior is explained by a time-averaged effective potential of the periodically driven system, which becomes double-well shaped under strong driving and thereby induces bistability with respect to the center of motion. Once the center of motion converges to either of the two local minima of the effective potential, inversion symmetry breaking occurs, giving rise to even-order harmonic generation despite the centrosymmetric nature of the original system. We show that the time-averaged position of the particle can be switched between the bistable points by additional control pulses. Conditions under which subharmonic generation occurs are also discussed. The demonstrated inversion symmetry breaking by periodic driving may lead to a scheme for manipulating localized particles and nonlinear optical responses that are inaccessible in the near-equilibrium regime.

DOI: 10.1103/trtr-9173

I. INTRODUCTION

Understanding the behavior of a system driven out of equilibrium by a time-periodic force is one of the central issues in the research of nonequilibrium phenomena. One intriguing prospect is the dynamical control of material properties and the realization of novel quantum phases that are absent in equilibrium—a concept recently termed "Floquet engineering" [1–7]. Experiments in ultracold atomic gases have proven the effectiveness of this concept by demonstrating dynamic control of, e.g., the matter-wave tunneling [8], quantum phase transition [9], artificial magnetic fields and spin interactions [10,11], and topological properties [12–16]. Floquet engineering has also been applied to solid-state systems, and various captivating phenomena have been theoretically proposed, as exemplified by optical control of topological properties and quantum degrees of freedom [17–25]. Experimentally, Floquet-Bloch states have been identified in the surface states of topological insulators and in semiconductors through time- and angle-resolved photoemission spectroscopy [26–31]. Coherent modulations of the material's properties by laser fields have recently been examined. Light-induced modulation of linear and nonlinear optical properties has been observed in semiconductors, insulators, and semimetals [32–35]. Light-induced anomalous Hall conductivity has been reported in graphene [36] and a Dirac semimetal [37], and is attributed to the modulation of the band topology.

Although Floquet engineering inherently relies on a quantum-mechanical description based on the Floquet theory, a simple classical approach can often capture the essence of the nonequilibrium dynamics under periodic driving. A well-known example is the Kapitza's pendulum, in which a high-frequency vibration stabilizes the pendulum at an inverted position that is unstable in equilibrium [38]. Kapitza's pendulum vividly demonstrates how periodic driving can modify the potential landscape of a system and is often referred to as an intuitive introduction to Floquet engineering.

Such a modified potential in a periodically driven system may lead to a symmetry distinct from that in equilibrium. Recent experiments have reported second-harmonic generation of infrared or terahertz pulses from centrosymmetric superconductors [39–41], although the interpretations provided in those works do not explicitly employ the Floquet formalism. The second-harmonic generation observed in Ref. [39] has been attributed to the dynamics of magnetic vortices trapped in a short-range pinning potential and driven by an oscillating Lorentz force induced by the terahertz current. A similar setup has been used to explain the nonmonotonic switching between the superconducting and normal states observed in Ref. [42]. These results suggest that exotic phenomena may arise when a particle in an anharmonic potential is exposed to strong periodic driving.

In this study, we demonstrate a prominent example of such nontrivial dynamics: Spatial inversion symmetry is broken by

*Contact author: sekiguchi@crc.u-tokyo.ac.jp

†Contact author: shimano@phys.s.u-tokyo.ac.jp

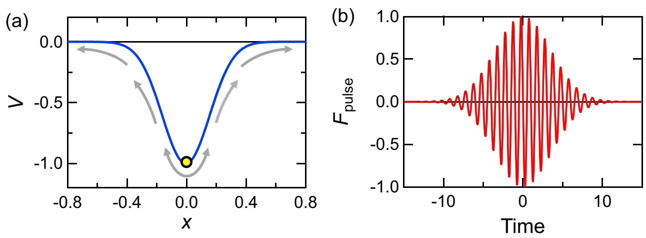

FIG. 1. (a) An inverted Gaussian potential $V(x)$ where a particle is trapped and (b) a pulsed oscillating force $F_{\mathrm{pulse}}(t)$ used in the simulation.

ac-pulse driving even in a centrosymmetric system, giving rise to even-order nonlinear responses that are forbidden by symmetry in equilibrium. To elucidate the essential behavior of a periodically driven particle, here we adopt a minimal model. We simulate the dynamics of a particle in an inverted Gaussian potential driven by a time-periodic external force. In Sec. II, we consider a pulsed oscillating force and show that, under strong driving, the center of oscillatory motion shifts away from the bottom of the trap potential, exhibiting bistable behavior. To clarify the underlying mechanism, we employ a ramped oscillating force in Sec. III and analyze the properties of the resulting steady-state oscillation. The time-averaged effective potential responsible for the bistability is explicitly calculated in Sec. IV. In Sec. V, we discuss the implications of the effective potential, namely, the convergence to the local minima of the effective potential and the switching between them by additional pulsed forces. We also demonstrate that the emergent inversion symmetry breaking gives rise to even-order nonlinear responses to additional perturbations. Finally, in Sec. VI, we discuss the possible observation of subharmonic generation. We summarize our results in Sec. VII.

II. DYNAMICS DRIVEN BY PULSED OSCILLATING FORCE

In the simulation, we apply an oscillating force to a particle initially at rest in the inverted Gaussian potential [Fig. 1(a)]. At the initial state, the particle is located at position $x = 0$ with velocity $v = 0$, and the external force is gradually introduced. First, we consider applying a pulsed oscillating force, as depicted in Fig. 1(b), to emulate experimental conditions relevant to laser-pulse-induced phenomena. Intense ultrafast laser pulses are powerful tools for driving matter into nonequilibrium states and have been widely used in experiments on condensed-matter systems. The present setup corresponds, for example, to a magnetic vortex in a pinning potential driven by a Lorentz force generated by a terahertz oscillating current, or more generally, to an electron confined in an impurity potential and driven by an optical field.

We simulate the dynamics by numerically solving the classical equation of motion, which reads

$$m_0\frac{d^2x}{dt^2} = F_{\mathrm{pulse}} - \frac{dV}{dx} - m_0\gamma\frac{dx}{dt}, \tag{1}$$

$$V(x) = -V_0 \exp\left[-\frac{x^2}{2\alpha^2}\right], \tag{2}$$

$$F_{\mathrm{pulse}}(t) = F_0 \sin(-\omega t)\exp\left[-\left(\frac{t}{\tau}\right)^2\right], \tag{3}$$

where $V(x)$ is the inverted Gaussian trap potential with the depth V_0 and the width α. $F_{\mathrm{pulse}}(t)$ is the pulsed oscillating force with a Gaussian envelope, where F_0 is the peak amplitude, ω is the angular frequency, and τ is the pulse duration. We also include a relaxation term by introducing a viscous drag coefficient γ. A similar setup without a relaxation term ($\gamma = 0$) has been analyzed in previous studies of atomic systems exposed to strong laser fields, where the suppression of ionization in the superintense-field regime has been predicted [43–45]. In the absence of friction, however, the system tends to exhibit chaotic dynamics, which prevents systematic investigation of symmetry breaking and associated harmonic generation. In this study, a finite relaxation constant is introduced to account for dissipation, which is ubiquitous in condensed matter. The inclusion of a friction term smoothens the dynamics, allowing us to capture the essential features of the nonlinear response and to interpret them intuitively in terms of spatial inversion symmetry breaking. We analyze the dynamics in the classical regime and discuss the resulting nontrivial behavior.

Below, we adopt $m_0 = 1$, $V_0 = 1$, $\alpha = 1/2\pi$, $\gamma = 1$, $\tau = 5$, unless otherwise mentioned. We set the driving frequency $\omega/2\pi = 1$, which is in resonance with the natural frequency of the harmonic oscillation around the potential minimum at the origin. The dependence of the dynamics on each parameter will be discussed later.

Figures 2(a)–2(d) show the time evolution of the particle's position x calculated for different amplitudes of the external force F_0. When F_0 is sufficiently small, the particle oscillates in the vicinity of the potential minimum. In this regime, the particle experiences a nearly harmonic potential, and thus exhibits sinusoidal oscillations with a Gaussian envelope, as shown in Fig. 2(a). This leads to an equal distribution of x in the positive and negative regions. However, as F_0 increases, qualitatively different dynamics appear. As shown in Fig. 2(b), the center of oscillatory motion shifts toward the positive direction at $F_0 = 21$. With a further increase of F_0, the oscillation amplitude first recovers a nearly symmetric shape at $F_0 = 23.4$ [Fig. 2(c)], and then the oscillation center shifts toward the negative direction at $F_0 = 28$ [Fig. 2(d)]. These results suggest the emergence of symmetry breaking in the driven system, raising a possibility of a counterintuitive phenomenon; when a particle trapped in a *centrosymmetric* potential is irradiated by a linearly polarized light, *even*-order harmonics can be generated.

Figure 2(e) shows the Fourier spectrum of the velocity at $F_0 = 28$. Indeed, when the particle exhibits polarized oscillation, even-order harmonic generation, including a rectification effect, can be discerned, despite the original system being centrosymmetric. We note that this symmetry breaking does not originate from a tailored configuration of the driving force, for example, as proposed in Refs. [46–50].

To quantitatively analyze the emergence of symmetry breaking, we evaluate the quasistatic displacement of the particle defined by

$$x_{\mathrm{ave}} = \int_{-\tau}^{\tau} x(t)dt/2\tau. \tag{4}$$

For the case of the pulsed force, x_{ave} is calculated as the time average of x while the pulsed force is applied [the shaded time region in Fig. 2(d)]. Figure 2(f) shows x_{ave} as a function

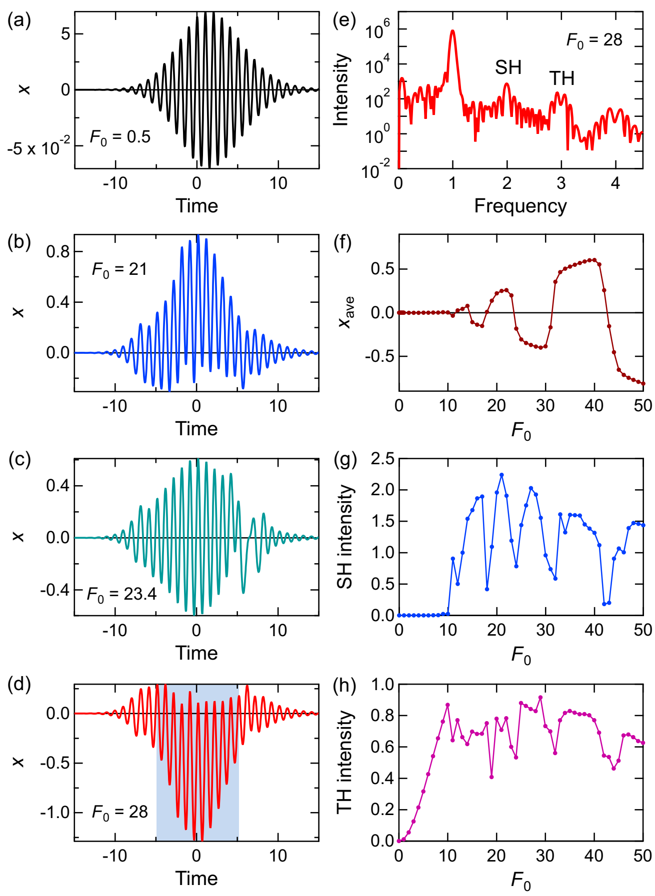

FIG. 2. The position $x(t)$ of the particle driven by $F_{\rm pulse}$ with (a) $F_0 = 0.5$, (b) $F_0 = 21$, (c) $F_0 = 23.4$, and (d) $F_0 = 28$. (e) Fourier spectrum of $v(t)$ at $F_0 = 28$. (f) F_0 dependence of $x_{\rm ave}$. F_0 dependence of (g) the second-harmonic intensity and (h) the third-harmonic intensity.

of F_0, where several interesting characteristics are identified. As seen earlier, $x_{\rm ave} = 0$ in the small-F_0 region; i.e., the oscillation motion is symmetric. On the other hand, a finite $x_{\rm ave}$ appears above a threshold around $F_0 = 9$. As F_0 increases further, the magnitude of $x_{\rm ave}$ grows while occasionally switching its polarity (positive or negative). The growth curve of $x_{\rm ave}$ appears to follow a certain envelope. Figures 2(g) and 2(h) show the intensities of the second harmonic (SH) and the third harmonic (TH), respectively, as a function of F_0. While the SH intensity remains zero in the small-F_0 region, it emerges above the threshold for producing a finite $x_{\rm ave}$. In contrast, the TH intensity continuously grows from $F_0 = 0$ and saturates in the large-F_0 region.

III. DYNAMICS DRIVEN BY RAMPED OSCILLATING FORCE

We now discuss the mechanism that leads to this ac field-driven symmetry breaking. Under the pulsed oscillating force, the dynamics is inherently transient and a steady state cannot be reached, which complicates the stability analysis of the particle's trajectory. Therefore, in the following, we employ a ramped oscillating force, as shown in Fig. 3(a), where the

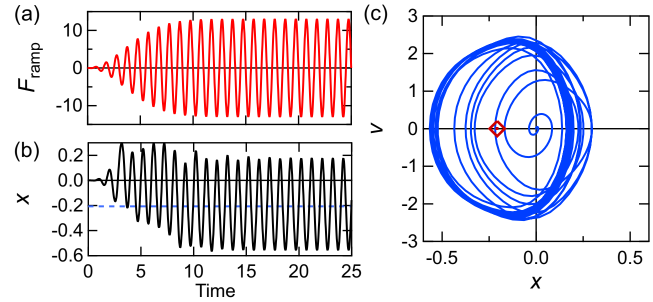

FIG. 3. (a) Ramped oscillating force $F_{\rm ramp}(t)$. (b) $x(t)$ driven by $F_{\rm ramp}$ with $F_0 = 13$. (c) Corresponding trajectory of $(x(t), v(t))$ in phase space. The dashed line in panel (b) and the diamond in panel (c) indicate the time-averaged position $x_{\rm ave}$ over one period of the steady oscillation.

time-periodic force is gradually ramped up. This form of the external force enables a smooth evolution from the initial state to the steady state of the particle's forced oscillation, as described in detail later, thereby allowing us to analyze the properties of the steady oscillation. Note that this setup emulates experimental conditions in which a continuous external force (such as a continuous-wave laser field) is ramped up from zero for a particle initially at rest.

The external force is given by

$$F_{\rm ramp}(t) = F_0 \sin(-\omega t)\left(1 - \exp\left[-\left(\frac{t}{\tau}\right)^2\right]\right), \qquad (5)$$

whose amplitude is ramped up over a time constant τ and then maintained at a constant amplitude of F_0 [Fig. 3(a)]. Figure 3(b) shows a typical time evolution of x calculated with $F_0 = 13$, where a steady state of the forced oscillation is reached in the late-time region. As in the case of the pulsed force, the center of motion is shifted away from the origin when F_0 is sufficiently large. Figure 3(c) illustrates the dynamics of the particle in phase space; i.e., the trajectory is plotted in the two-dimensional space spanned by x and v. The realization of a steady oscillation corresponds to convergence to a closed trajectory in phase space, namely, a limit cycle. The center of the limit cycle, which we define as the time-averaged position $x_{\rm ave}$ over one period of the steady oscillation, is displaced from the origin [Fig. 3(c)].

To analyze the convergence to a limit cycle, we compute the stroboscopic map of the periodically driven system. In the stroboscopic map, starting from an initial state $(x(t_0),\ v(t_0))$ in phase space, we calculate the time evolution over one period of the external force to obtain the final state $(x(t_0 + T),\ v(t_0 + T))$, where $T = 2\pi/\omega$. We then examine the phase-space difference $\Delta P = (x(t_0 + T) - x(t_0),\ v(t_0 + T) - v(t_0))$. If $\Delta P = 0$, the point $(x(t_0),\ v(t_0))$ lies on the trajectory of a limit cycle. Since we are interested in the properties of the steady state at the late-time region, we use a sinusoidal oscillation as the external force (after the ramping of $F_{\rm ramp}$ has been completed). The initial time t_0 is arbitrary, and we set $t_0 = 0$.

In Fig. 4, the magnitude and the direction of ΔP are mapped onto the phase space. When F_0 is sufficiently small, as shown in Fig. 4(a), there exists a point near $x = 0$ where

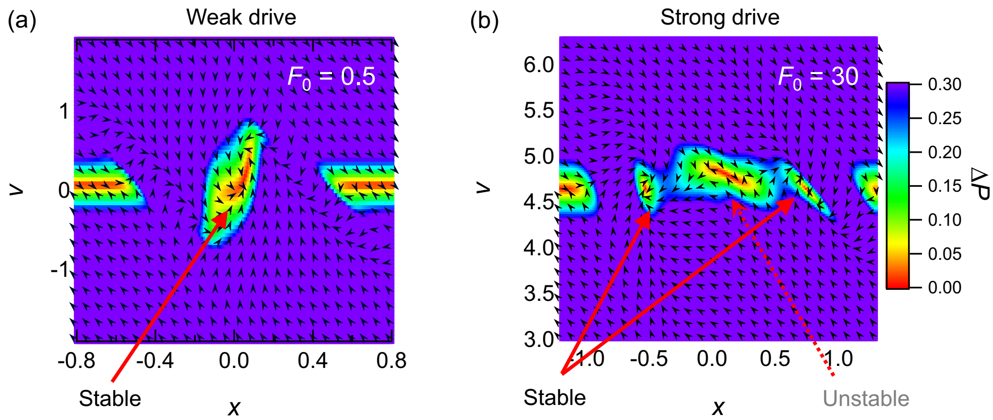

FIG. 4. Stroboscopic map of the phase-space difference, $\Delta P = (x(t_0 + T) - x(t_0),\ v(t_0 + T) - v(t_0))$, calculated for (a) $F_0 = 0.5$ and (b) $F_0 = 30$.

the magnitude of ΔP is zero, indicating the presence of a limit cycle. The surrounding ΔP arrows converge toward this point, indicating that any trajectory starting from its vicinity approaches this point after one period. Therefore, the corresponding limit cycle is an attractor, which is robust against perturbations. Figure 4(a) shows that the system possesses a single stable limit cycle under weak driving, which corresponds to the harmonic oscillation. The red regions ($\Delta P = 0$) on the positive and negative x sides in Fig. 4(a) are not relevant because they represent trajectories of the forced oscillation in free space, starting from the initial state outside the trap potential. Although these trajectories also form limit cycles, they are not stable against perturbations.

The property of the limit cycle changes qualitatively under strong driving. As shown in Fig. 4(b), although there remains a region of $\Delta P = 0$ near $x = 0$, the ΔP arrows no longer converge toward this point, indicating that it corresponds to an unstable limit cycle. Instead, two red regions appear on both sides of the unstable limit cycle near the origin, and the ΔP arrows point toward these regions, indicating the emergence of two stable limit cycles. These results reveal that the stability of the limit cycles depends on the driving strength: while a single stable limit cycle exists under weak driving, strong driving gives rise to two stable limit cycles (bistability).

To investigate how this bistability emerges, we evaluate x_{ave} for the steady oscillations at different driving strengths to determine the center of motion of the limit cycles. Here, x_{ave} is defined as the time-averaged position over one period of the steady oscillation. Figure 5 shows x_{ave} as a function of F_0. The sign of x_{ave} in the steady state depends on the sinusoidal phase of the external force, while its magnitude remains unchanged. For a clearer view of the emergence of the bistability, Fig. 5 shows the results calculated with driving phases of 0 and π superimposed. In the weak-driving regime, $x_{\mathrm{ave}} = 0$, indicating the oscillation center lies at the origin. This is because the particle oscillates near the bottom of the potential, where the potential is almost harmonic. However, as F_0 increases and exceeds a threshold at $F_0 \sim 9$, a pitchfork bifurcation occurs: The oscillation center splits into two branches in the positive and negative regions. These two branches embody the bistability of the limit cycles observed in Fig. 4(b). As shown in Fig. 5, since the Gaussian trap potential is isotropic, the bistable branches appear symmetrically with respect to the origin, and the displacement increases monotonically with F_0. The displacement of the oscillation center persists without saturation, and hence x_{ave} grows beyond the width of the Gaussian trap potential ($\sqrt{2}\alpha = 0.23$).

In light of this emergent bistability, we can now interpret the dynamics under the pulsed oscillating force observed in Fig. 2. When driven strongly, two symmetric centers of motion appear in the positive and negative x regions. The stabilities of these two states are energetically equivalent, and the particle becomes displaced toward either the positive or negative region. The destination of the oscillation center is determined by the amplitude and phase of the driving force and depends on the viscous drag coefficient γ. Although the dynamics is deterministic, its dependence on these parameters is complicated and becomes chaotic at smaller γ. After the pulsed force ceases, the particle relaxes back to the bottom of the trap potential. Such an adiabatic following explains the seemingly counterintuitive motion observed in Fig. 2. Comparison between Figs. 2(f) and 5 suggests that the observed bifurcation behavior originates from the same underlying mechanism. Therefore, the key features of the behavior observed under the pulsed oscillating force can be

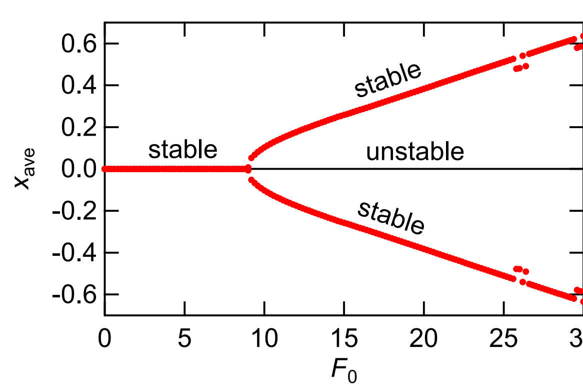

FIG. 5. F_0 dependence of x_{ave} calculated in the steady-state regime. Results for the driving phases of 0 and π in F_{ramp} are superimposed. $\tau = 15$.

consistently captured by investigating the steady oscillations induced by the ramped oscillating force.

IV. EFFECTIVE POTENTIAL CALCULATED BY THE TIME-AVERAGING METHOD

Through numerical calculations, we have found that bistable oscillation centers emerge under strong driving in the form of a pitchfork bifurcation. To elucidate the underlying mechanism, we calculate the time-averaged effective potential, which provides an intuitive insight into the behavior of the periodically driven system.

Here, our interest lies in the position of the oscillation center of the particle, which shifts slowly compared to the oscillation period of the external driving force, as shown in Fig. 3. To highlight the motion of the oscillation center, it is useful to decompose the dynamics of $x(t)$ into a fast component $\varepsilon(t)$, which oscillates at the same frequency as the external force, and a slow component $X(t)$, which describes the gradual shift of the oscillation center:

$$x(t) = X(t) + \varepsilon(t). \tag{6}$$

We then introduce a time-averaging operation over one period of the external force,

$$\langle x(t)\rangle_T = \frac{1}{T}\int_{t-\frac{T}{2}}^{t+\frac{T}{2}} x(t')dt', \tag{7}$$

which effectively coarse grains the motion over the time $T = 2\pi/\omega$. Under this averaging, the fast component $\varepsilon(t)$ and its derivatives vanish, while the slow component $X(t)$ and its derivatives remain unchanged:

$$\langle\ddot{\varepsilon}(t)\rangle_T = \langle\dot{\varepsilon}(t)\rangle_T = \langle\varepsilon(t)\rangle_T = 0, \tag{8}$$

$$\langle\ddot{X}(t)\rangle_T = \ddot{X}(t), \tag{9}$$

$$\langle\dot{X}(t)\rangle_T = \dot{X}(t), \tag{10}$$

$$\langle X(t)\rangle_T = X(t), \tag{11}$$

$$\langle F(t)\rangle_T = 0. \tag{12}$$

Consequently, the original equation of motion can be reformulated in terms of $X(t)$, resulting in

$$m_0\ddot{X}(t) + m_0\gamma\dot{X}(t) = \left\langle -\frac{d}{dX}V(X(t)+\varepsilon(t))\right\rangle_T. \tag{13}$$

Equation (13) can be interpreted as describing the dynamics of $X(t)$ under a force derived from a time-averaged effective potential. In evaluating the right-hand side of Eq. (13), we assume that the variation of $X(t)$ during one cycle of the external force is negligibly small compared to that of $\varepsilon(t)$, and hence approximate $X(t)$ as constant during the time-averaging operation. With this approximation, the right-hand side of Eq. (13) can be written as

$$-\frac{dV_{\text{eff}}}{dX} \sim \left\langle -\frac{d}{dX}V(X+\varepsilon(t))\right\rangle_T. \tag{14}$$

Equation (14) indicates that the force derived from the effective potential is given by the time-averaged force exerted by the original potential over one oscillation cycle of the particle around the position X. The time-averaging operation in Eq. (14) can be transformed into a spatial convolution of the original force [Fig. 6(a)] with an appropriate weighting function through a change of variables. The weighting function, or "density of states," corresponds to the dwell time, i.e., the amount of time the particle spends at each position x during one oscillation cycle.

To proceed, we rewrite Eq. (14) with a further approximation. Although an analytic solution for the rapidly oscillating component $\varepsilon(t)$ is not available, it exhibits a nearly sinusoidal oscillation with period T, as confirmed in Fig. 3. We therefore approximate it by a simple sinusoidal motion with amplitude σ,

$$\varepsilon(t) = \sigma\sin(\omega t + \delta). \tag{15}$$

When $\varepsilon(t)$ is sinusoidal, the weighting function can be expressed as

$$\rho(x) = \frac{1}{\pi\sqrt{1-x^2}}, \tag{16}$$

which is shown in Fig. 6(b). Under these approximations, Eq. (14) can be rewritten as

$$-\frac{dV_{\text{eff}}(X)}{dX} = -\int_{X-\sigma}^{X+\sigma} \rho\left(\frac{x'-X}{\sigma}\right)\frac{dV(x')}{dx'}dx' \tag{17}$$

It should be noted that the particle spends the least time at the center of oscillation and the most time at the turning points during the oscillatory motion. Consequently, the weighting function given by Eq. (16) takes its minimum at the center and reaches its maximum at the edges. This characteristic of the weighting function plays a crucial role in determining the effective potential in the periodically driven system. Since Eq. (17) provides the derivative of the effective potential, we integrate it to obtain the effective potential in real space.

The calculated results are shown in Figs. 6(c) and 6(d). Figure 6(c) represents the derivatives (i.e., the effective force), and Fig. 6(d) shows the effective potential in real space. For a small oscillation amplitude ($\sigma = 0.2$), the width of the weighting function is narrow, and hence the shape of the effective potential does not deviate significantly from that of the original potential. Indeed, the curves for $\sigma = 0.2$ exhibit a slightly broadened Gaussian-like shape. At a larger oscillation amplitude ($\sigma = 0.3$), the bottom of the effective potential becomes increasingly flat. At an even larger amplitude ($\sigma = 0.5$), the origin turns into an unstable point, and new local minima emerge around $x = \pm 0.35$. Consequently, the effective potential takes on a double-well shape. The newly developed potential minima correspond to the bistable centers of motion observed in the numerical simulations. Figure 6(e) shows the more detailed σ dependence of $V_{\text{eff}}(X)$. The local minima of the double-well potential appear through a bifurcation, as shown in Fig. 6(f). The depth of the potential trap (activation energy necessary for hopping to the other minimum) and natural frequency around the local minima develop nonmonotonically as functions of F_0 [Figs. 6(g) and 6(h)].

To assess the validity of the time-averaged effective potential, the local minima of $V_{\text{eff}}(X)$ are compared with the

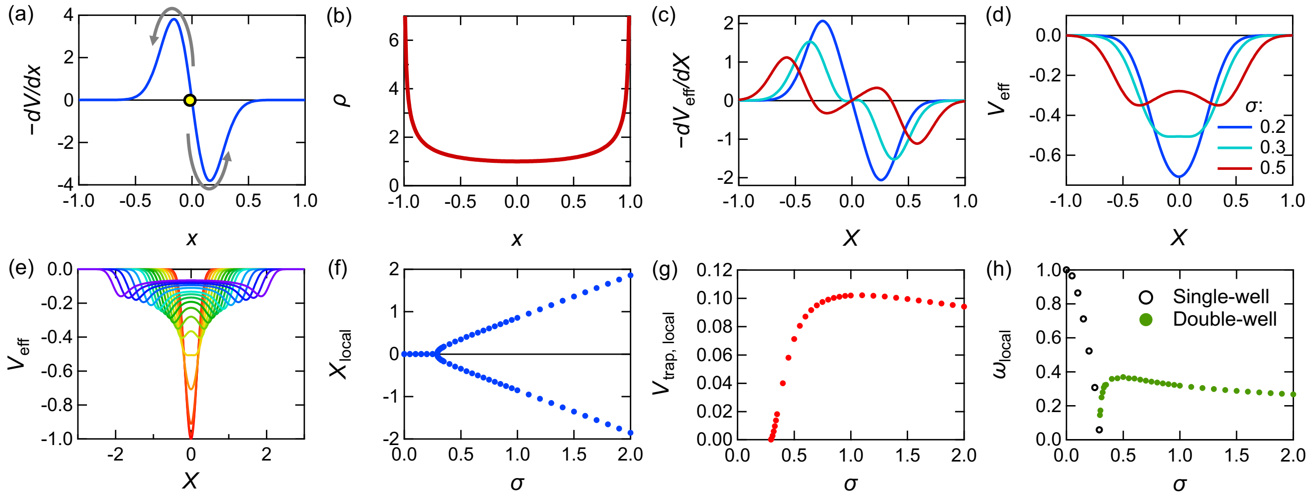

FIG. 6. (a) Spatial derivative of the original inverted Gaussian potential $-dV(x)/dx$. (b) Weighting function $\rho(x)$. (c) Effective force derived from the time-averaged potential $-dV_{\mathrm{eff}}(X)/dX$ calculated with different oscillation amplitudes σ. (d) Corresponding landscape of the effective potential $V_{\mathrm{eff}}(X)$. (e) $V_{\mathrm{eff}}(X)$ calculated for different values of σ, from $\sigma = 0$ to $\sigma = 2$. σ dependence of (f) the position, (g) the trap depth (activation energy required for hopping to the other minimum), and (h) the natural frequency derived from the curvature at the local minima of $V_{\mathrm{eff}}(X)$.

numerically calculated x_{ave} in Fig. 7(b). For this comparison, a conversion between F_0 and σ, i.e., between the amplitude of the external force and that of the steady oscillation, is required. Here, σ denotes the amplitude of a sinusoidal oscillation that approximates the steady-state motion. To establish the relation between F_0 and σ, we assume that $\sigma = (x_{\mathrm{max}} - x_{\mathrm{min}})/2$, where x_{max} and x_{min} are the maximum and minimum values of x over one cycle of the steady oscillation, and evaluate its dependence on F_0. The result is shown in Fig. 7(a), which provides the conversion function between F_0 and σ. Using this relation, the plot in Fig. 7(b) is obtained. Although a slight deviation is observed in the threshold value of F_0, the effective potential well reproduces the numerically obtained bifurcation behavior of the steady oscillation.

We now give an intuitive explanation for why the effective potential changes to a double-well form under strong driving. As mentioned earlier, during the oscillatory motion, a particle spends less time near the center and more time near the edges. Then, consider a question: Under a forced oscillation with a given amplitude, where should the center of oscillation be located to minimize the energy cost? The answer can be found by comparing Figs. 8(a) and 8(b). When the oscillation amplitude is sufficiently large, the total energy over one cycle can be reduced by shifting the center of oscillation either toward the positive or negative side [Fig. 8(b)] to make the particle stay longer at the bottom of the original potential. This energetic advantage accounts for the emergence of bistable oscillation centers that are symmetrically displaced from the origin.

V. IMPLICATIONS OF THE EFFECTIVE POTENTIAL

Hitherto, we have calculated the effective potential that describes the center of the steady-state forced oscillation. However, it is nontrivial whether the center of motion, starting from the initial state ($x = 0$, $v = 0$), always reaches one of the bistable minima of the effective potential. In other words, it is not guaranteed that a trajectory converges to a stable limit cycle of the driven system.

In this study, we consider the dynamics of a particle that is initially at rest at the origin ($x = 0$, $v = 0$) and is driven by the external force ramped up from zero over a finite rise time τ. In the following, we demonstrate that τ has a crucial influence on the destination of the trajectory, i.e., which steady state the system eventually reaches.

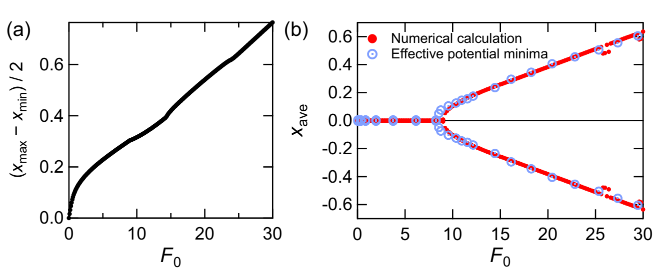

FIG. 7. (a) F_0 dependence of the steady-state oscillation amplitude, $(x_{\mathrm{max}} - x_{\mathrm{min}})/2$. (b) Comparison between the local minima of $V_{\mathrm{eff}}(X)$ and the numerically calculated x_{ave}. In plotting the F_0 dependence of the local minima of the effective potential, we assume that σ in Fig. 6(f) corresponds to $(x_{\mathrm{max}} - x_{\mathrm{min}})/2$ in panel (a).

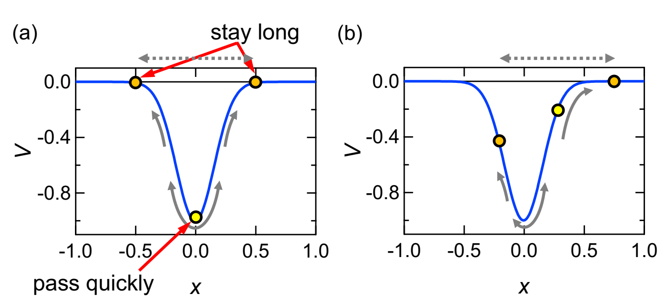

FIG. 8. Schematic drawing of the steady oscillation with the center (a) located at the origin and (b) shifted away from the origin.

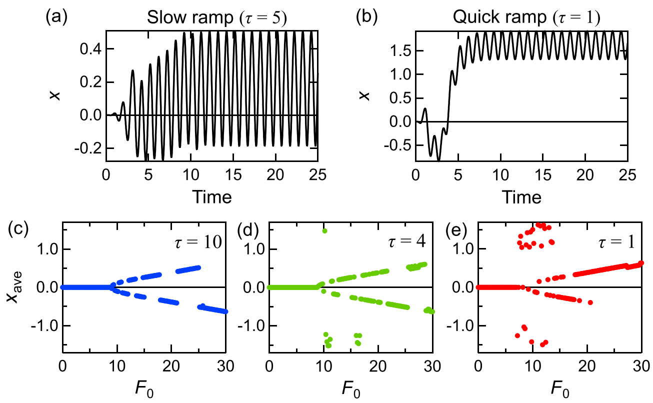

FIG. 9. $x(t)$ calculated with $F_0 = 12$ and with rise times of (a) $\tau = 5$ and (b) $\tau = 1$. F_0 dependence of x_{ave} calculated with (c) $\tau = 10$, (d) $\tau = 4$, and (e) $\tau = 1$.

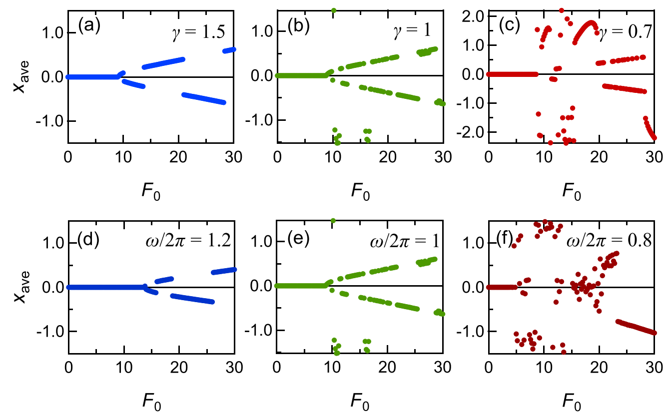

FIG. 10. γ dependence of x_{ave}, calculated with (a) $\gamma = 1.5$, (b) $\gamma = 1$, and (c) $\gamma = 0.7$. ω dependence of x_{ave}, calculated with (d) $\omega/2\pi = 1.2$, (e) $\omega/2\pi = 1$, and (f) $\omega/2\pi = 0.8$. For the calculations shown in panels (a)–(f), a rise time of $\tau = 4$ is used, and $\omega/2\pi = 1$ in panels (a)–(c), and $\gamma = 1$ in panels (d)–(f).

Figures 9(a) and 9(b) compare the dynamics under different rise times, while keeping other parameters fixed. In Fig. 9(a), where the external force is ramped up slowly ($\tau = 5$), a steady oscillation around $x = 0.18$ appears, which corresponds to one of the stable points in the effective potential for $F_0 = 12$. In contrast, when the external force is ramped up rapidly (with $\tau = 1$), as shown in Fig. 9(b), the particle escapes from the trap potential and oscillates in free space. In this case, the particle fails to reach the bistable points of the effective potential. The destination of the trajectory in Fig. 9(b) corresponds to the red region extending to the positive side in Fig. 4(b), i.e., an unstable limit cycle.

The dependence on τ is summarized in Figs. 9(c)–9(e), where the time-averaged position x_{ave} (evaluated over $t =$ 120–150) is plotted as a function of F_0 for different values of τ. When the external force is ramped up slowly, the particle always reaches one of the bistable states, and the bifurcation curve can be clearly identified, as shown in Fig. 9(c). On the other hand, when the field is ramped up quickly, as shown in Figs. 9(d) and 9(e), the particle is prone to escaping to free space. In other words, the trajectory frequently fails to converge to the bistable minima of the effective potential. These results indicate that, to ensure a smooth transition from the static state of an undriven system to a stable steady state of the driven system, it is crucial to introduce the external force gradually, in an adiabatic manner.

The connectivity to the bistable steady state also depends on parameters other than τ. Figures 10(a)–10(f) show plots similar to Fig. 9, where the dependences on the viscous drag (friction) constant γ and the driving frequency ω are examined. In Figs. 10(a)–10(c), x_{ave} is calculated using different values of γ, while other parameters are fixed. The results show that larger friction leads to better convergence to the bistable states, even under the same rise time of F_{ramp}. Similarly, Figs. 10(d)–10(f) show that detuning the driving frequency toward higher frequencies improves convergence to the bistable states. These results indicate that "smoother" dynamics, achieved by larger friction or higher driving frequency, facilitate connection to the bistable points of the effective potential of the driven system. For a complementary perspective, the detailed dependence on these parameters is shown in Fig. 11, where the deviation of x_{ave} in the steady oscillation from the bistable point is plotted as a function of τ, γ, and ω. The calculations were performed with $F_0 = 12$. In our simulation, the steady state was found to be sensitive to the initial conditions of the external driving. In other words, the steady oscillation is not uniquely determined unless the initial state is specified, which can be a crucial factor in real experiments. Simulations employing a ramped force naturally incorporate this aspect. In Fig. 11, results for $\phi = 0$, 0.2π, 0.4π, 0.6π, and 0.8π are plotted simultaneously, where ϕ denotes the phase of the external force. Here, a finite value on the vertical axis indicates a failure to converge to the bistable points. Figure 11 demonstrates that a longer τ, larger γ, and higher ω configuration facilitates convergence to the bistable points. Overall, these results emphasize that the bistable state under periodic driving is not trivially reached and critically depends on the dynamical properties of the driven system.

The dependence of harmonic generation on the system parameter is examined in Fig. 12. Figures 12(b) and 12(c) compare the harmonic intensities generated from the steady oscillation, calculated with $\gamma = 0.7$ and 2. Although we adopted a long rise time of $\tau = 30$, x_{ave} sometimes fails to converge to the bistable points in the case of $\gamma = 0.7$. When the particle escapes from the trap potential, it oscillates in free space, and consequently, no harmonics are generated.

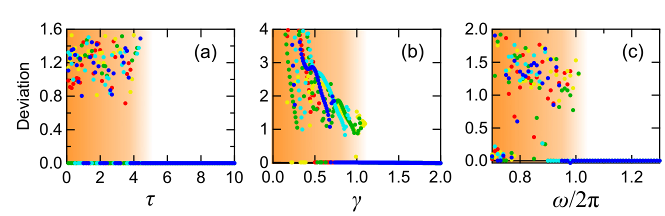

FIG. 11. Dependence of the deviation of x_{ave} from the bistable points on (a) τ, (b) γ, and (c) ω. Different colors represent results obtained for different phases of the external driving force. The calculations were performed with (a) $F_0 = 12$, $\gamma = 1$, $\omega = 1$; (b) $F_0 = 12$, $\tau = 4$, $\omega = 1$; and (c) $F_0 = 12$, $\tau = 4$, $\gamma = 1$.

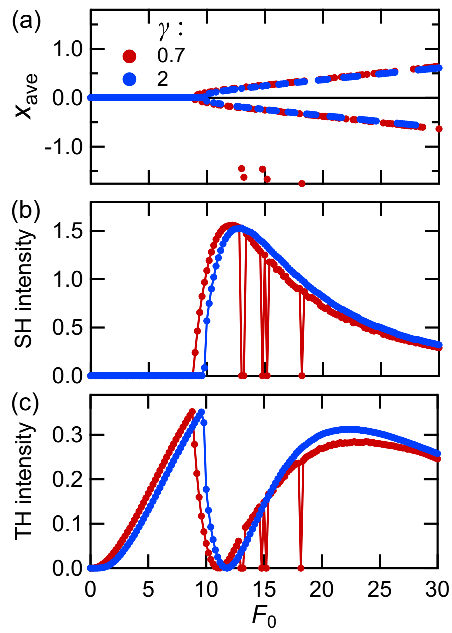

FIG. 12. F_0 dependence of (a) $x_{\rm ave}$ and the intensity of (b) the second and (c) the third harmonics generated from the steady oscillation. The calculations were performed with $\tau = 30$, $\omega/2\pi = 1$, and $\gamma = 0.7$ or 2.

Indeed, the SH and TH intensities fall to zero when $x_{\rm ave}$ fails to converge to the bistable points [compare Fig. 12(a) with Figs. 12(b) and 12(c)]. Apart from this behavior, the F_0 dependence of the SH and TH intensities does not show a significant difference between $\gamma = 0.7$ and 2. Since a larger γ leads to a smaller amplitude of the steady oscillation, the threshold for the pitchfork bifurcation slightly increases at larger γ, which in turn affects the emergence of SH in Fig. 12(b).

Under appropriate conditions for $F_{\rm ramp}$, the center of motion of the particle converges to one of the bistable points in the effective potential. In the absence of other perturbations, these bistable points are energetically equivalent, and the destination of the particle is determined by the parameters of the system in a nontrivial manner. This raises another question of whether it is possible to switch between these bistable points afterward. To examine this possibility, we apply another pulsed stimulus to the periodically driven particle. First, $F_{\rm ramp}$ with $F_0 = 12$ is ramped up at $t = 0$ so that the bistable steady state is reached. Then, we apply a control pulse

$$F_{\rm c}(t) = F_1 \sin(-\Omega(t - t_d))\exp\left[-\left(\frac{t - t_d}{\tau}\right)^2\right]. \tag{18}$$

Here, we adopt a small amplitude of $F_1 = 1$ and a relatively low frequency of $\Omega = 0.75$, since the natural frequency around the local minima in $V_{\rm eff}(X)$ is relatively low, as shown in Fig. 6(h). $F_{\rm c}$ is applied at sufficiently later times, $t_d = 100$ and 200, as shown in Fig. 13(a). Figure 13(b) shows the simulated dynamics of the time-averaged position over one cycle of the external force $\langle x(t)\rangle$, calculated according to Eq. (7). After $F_{\rm ramp}$ is ramped up, $\langle x\rangle$ reaches one of the bistable points in the positive region at $t \sim 20$. Then, upon application of a control pulse $F_{\rm c}$ at $t = 100$, $\langle x\rangle$ jumps to another stable point

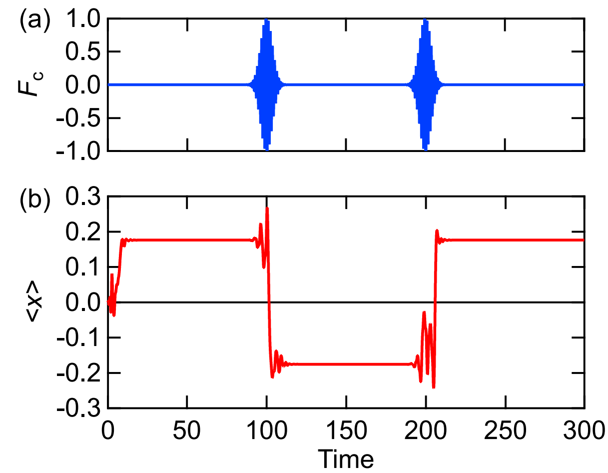

FIG. 13. (a) Control pulse $F_{\rm c}(t)$. (b) Time evolution of $\langle x(t)\rangle$ driven by $F_{\rm ramp} + F_{\rm c}$.

in the negative region. $\langle x\rangle$ remains constant until another $F_{\rm c}$ is applied, which again switches the sign of $\langle x\rangle$. This observation suggests that switching between the bistable points can be achieved by applying a weak pulsed force as a stimulus.

When the center of motion is shifted away from the origin, as schematically illustrated in Fig. 8(b), the periodic motion of the particle, i.e., the rapidly oscillating component $\varepsilon(t)$, becomes asymmetric between the positive and negative directions. This asymmetry in $\varepsilon(t)$ results in the generation of even-order harmonics of the driving frequency ω, as shown in Figs. 2(e) and 12(b). In this case, the slow component $X(t)$ stays localized at one of the minima of the double-well effective potential, where the potential landscape is locally asymmetric. Consequently, when the system is observed on a timescale much slower than ω, the periodic driving effectively induces properties associated with broken spatial inversion symmetry.

To examine the effect of the broken symmetry in the effective potential, we apply a low-frequency oscillating force $F_{\rm lf}$ on top of $F_{\rm ramp}$ and simulate the resulting dynamics. $F_{\rm lf}$ is given by

$$F_{\rm lf}(t) = F_1 \sin(-\Omega(t - t_d)) \times \left(1 - \exp\left[-\left(\frac{t - t_d}{\tau}\right)^2\right]\right) u(t - t_d), \tag{19}$$

where F_1 is the amplitude and $\Omega = 0.05$ is the frequency much smaller than $\omega = 1$ of $F_{\rm ramp}$. $u(t)$ denotes the unit-step function. In the simulation, $F_{\rm ramp}$ with $F_0 = 12$ is ramped up at $t = 0$, and $F_{\rm lf}$ is ramped up at a sufficiently later time, $t_d = 50$. As shown in Fig. 9(a), the steady state is already reached at $t = t_d$. After a sufficiently long time, the oscillatory motion in the new steady state is calculated. The Fourier spectra of $v(t)$ in the steady oscillation regime are shown in Fig. 14. As F_1 increases, higher harmonics, including even orders, continuously emerge. This perturbative even-order harmonic generation with respect to the additional pulse $F_{\rm lf}(t)$ manifests the inversion symmetry breaking of the driven system. Consequently, effective nonlinear susceptibilities for even-order harmonic generation become active in the periodically driven steady state due to the inversion symmetry breaking associ-

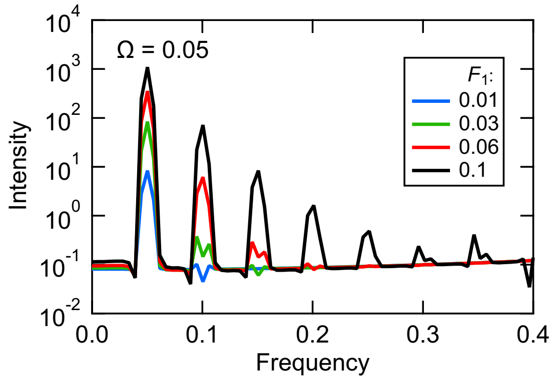

FIG. 14. Fourier spectra of $v(t)$ in the low-frequency region. The particle is driven by $F_{\mathrm{ramp}} + F_{\mathrm{lf}}$, and the results are calculated with different values of F_1.

ated with the local minima of the double-well-shaped effective potential. This phenomenon can be contrasted with the widely observed field-induced second-harmonic generation [51–53], where static external fields break the inversion symmetry of the system. In the present case, the rapidly oscillating external force does not have a fixed polarity, and the inversion symmetry is effectively broken only after the bistability emerges.

VI. SUBHARMONIC GENERATION

So far, we have focused on the bistability that emerges under strong periodic driving. There, we have assumed that the particle oscillates at the same frequency as, or at higher-order harmonics of, the driving force F_{ramp}. In the following, we demonstrate that more complex dynamics emerge for specific parameter values.

Figures 15(a), 15(d), and 15(g) show the dynamics of the time-averaged position $\langle x(t)\rangle$ at different amplitudes of F_{ramp}. The time averaging is performed according to Eq. (7), in the same manner as in Fig. 13(b). Figure 15(a) shows the dynamics at $F_0 = 12$, where $\langle x\rangle$ converges to one of the bistable points and remains constant at later times after $t \sim 20$. This indicates that the particle is in a steady oscillation around the local minimum of the effective potential, at the same frequency as or at integer-order harmonics of the driving frequency ($\omega = 1$). The Fourier spectrum of the velocity $v(t)$ in this steady oscillation [shaded time region in Fig. 15(a)] is plotted in Fig. 15(b), where peaks at the fundamental frequency and its higher-order harmonics can be identified. As explained earlier, this spectrum contains even-order harmonics, while the DC component is not included in the steady oscillation. The corresponding limit cycle in phase space is shown in Fig. 15(c).

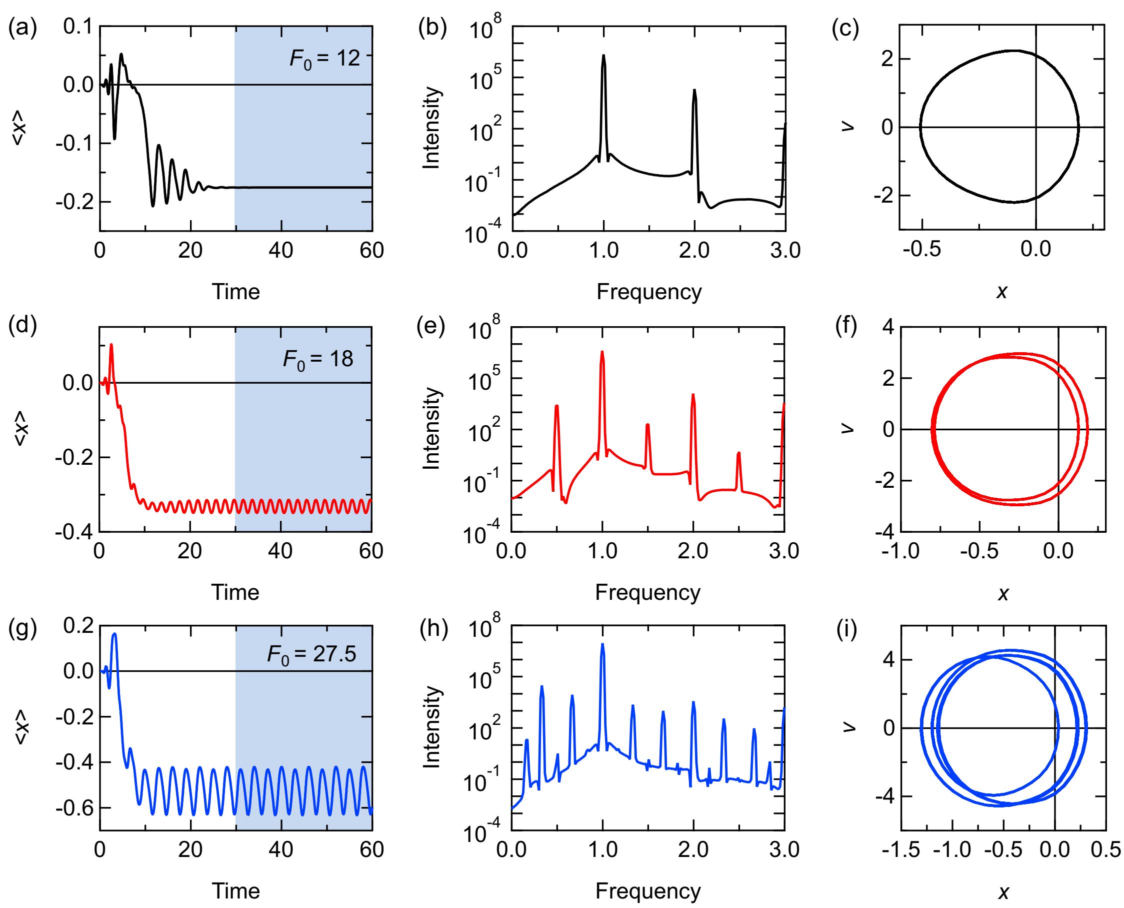

FIG. 15. Dynamics for (a)–(c) $F_0 = 12$, (d)–(f) $F_0 = 18$, and (g)–(i) $F_0 = 27.5$. (a), (d), (g) $\langle x(t)\rangle$. (b), (e), (h) Fourier spectrum of $v(t)$ for the steady oscillation and (c), (f), (i) limit cycle corresponding to the steady oscillation.

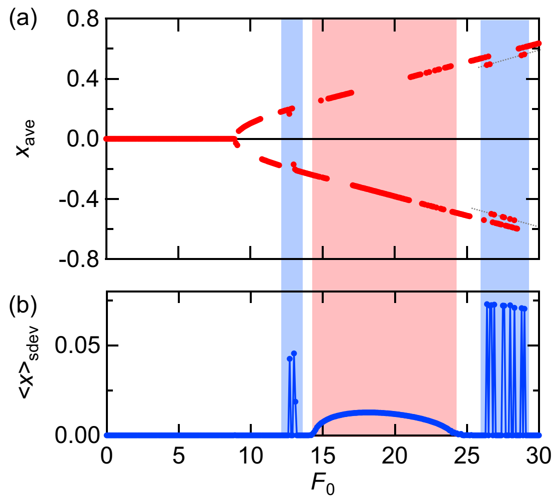

FIG. 16. F_0 dependence of (a) x_{ave} and (b) $\langle x\rangle_{\text{sdev}}$. The region where $(n/2)\omega$ and $(n/3)\omega$ harmonics appear are highlighted in red and blue, respectively.

On the other hand, $\langle x\rangle$ exhibits persistent oscillations at $F_0 = 18$ and 27.5, as shown in Figs. 15(d) and 15(g). This indicates that the steady oscillations contain frequency components that are noninteger multiples of the driving frequency. Indeed, the Fourier spectra of $v(t)$ of these steady oscillations show peaks at $(n/2)\omega$ for $F_0 = 18$ and $(n/3)\omega$ for $F_0 = 27.5$, as shown in Figs. 15(e) and 15(h), indicating the occurrence of *subharmonic* generation. The corresponding limit cycles in phase space are plotted in Figs. 15(f) and 15(i). For example, in the case of the dynamics containing $(n/2)\omega$ subharmonics, the trajectory closes after two cycles of the external force.

In Fig. 16, we visualize the parameter regions where subharmonics are generated. As seen in Fig. 15, when subharmonics are present, $\langle x(t)\rangle$ exhibits persistent oscillations, and therefore the standard deviation of $\langle x(t)\rangle$, $\langle x\rangle_{\text{sdev}}$, becomes finite in the steady state of forced oscillation [shaded time region in Figs. 15(a), 15(d), and 15(g)]. In contrast, if the dynamics contain only the fundamental frequency or integer-order harmonics, $\langle x\rangle_{\text{sdev}}$ becomes zero. Thus, $\langle x\rangle_{\text{sdev}}$ serves as an indicator of the presence of subharmonic components. Figures 16(a) and 16(b) show the F_0 dependence of x_{ave} and $\langle x\rangle_{\text{sdev}}$, respectively. A comparison between Figs. 16(a) and 16(b) reveals that subharmonics emerge in the F_0 region above the threshold of the pitchfork bifurcation.

The emergence of subharmonics is sensitively affected by the friction γ and the frequency detuning of the driving force. This system is prone to exhibiting chaotic dynamics for smaller γ and lower ω driving, and subharmonics tend to appear near the onset of such chaotic dynamics. In contrast, larger γ or higher ω driving suppresses subharmonic generation.

In Fig. 16, the region where $(n/3)\omega$ harmonics appear is highlighted in blue for eye guide. A close inspection of Fig. 16(a) reveals that, in the presence of $(n/3)\omega$ harmonics, x_{ave} appears slightly on the inner side of the bifurcated lines. This indicates that when $(n/3)\omega$ harmonic components emerge, the center of motion shifts from the local minima of the time-averaged effective potential.

Another important aspect of the $(n/3)\omega$ harmonics is that they are not robust against fluctuations. As seen in Fig. 16(b), the points with finite $\langle x\rangle_{\text{sdev}}$ are discrete; $(n/3)\omega$ subharmonics do not appear continuously as F_0 is varied. Similarly, the generation of $(n/3)\omega$ subharmonics is highly sensitive to fluctuations in the driving phase and the rise time of F_{ramp} (not shown), indicating that the dynamics is inherently unstable.

The region where the $(n/2)\omega$ harmonics appear is highlighted in red in Fig. 16. In contrast to the $(n/3)\omega$ case, the points with finite $\langle x\rangle_{\text{sdev}}$ appear continuously with changing F_0 in the red-shaded region. This indicates that the generation of $(n/2)\omega$ harmonics is robust against the fluctuations in F_0. It is also robust against fluctuations in the driving phase and rise time (not shown). In particular, $(n/2)\omega$ harmonics can be generated with a smooth ramp of F_{ramp} over a very long t. This suggests that the $(n/2)\omega$ harmonics are easier to detect experimentally. Such exotic harmonics may enable an unconventional approach to frequency division or down-conversion.

VII. SUMMARY

We investigated the dynamics of a particle initially trapped in an inverted Gaussian potential and driven by a time-periodic external force. While the motion of the particle is a symmetric sinusoidal oscillation under weak driving, the center of the oscillatory motion shifts away from the bottom of the potential under strong driving, toward either the positive or negative direction. To elucidate the underlying mechanism of this emergent spatial inversion symmetry breaking, we analyzed the properties of steady oscillations by simulating the system dynamics under a ramped oscillating force, revealing the emergence of bistable limit cycles through a pitchfork bifurcation. This bistability can be intuitively understood in terms of the time-averaged effective potential of the periodically driven system, which becomes double-well shaped under strong driving. The center of motion of the particle converges to either of these bistable minima, which can be switched by applying control pulses. Convergence to these local potential minima depends on parameters such as the rise time τ and frequency ω of the external force, and the viscosity γ. Our simulations also suggest that subharmonic generations occur under certain conditions. The emergent broken symmetry of the driven system could give rise to functionalities inaccessible in equilibrium. For example, periodic driving can effectively enable even-order nonlinear responses in centrosymmetric materials, providing a mechanism for even-order harmonic generations and inducing quasistatic polarizations or rectified currents. Subharmonic generation may offer an alternative approach to frequency (photon energy) conversion. The convergence to, and switching between, the bistable centers of motion may provide a scheme for manipulating localized particles. While we have adopted a Gaussian shape for the trap potential, a similar behavior is also observed with a Lorentzian potential, suggesting that our findings are universal for short-range trap potentials.

ACKNOWLEDGMENTS

We thank N. Yoshikawa, S. A. Sato, Y. Murakami, and T. Shirai for fruitful discussions. This work was supported by JSPS KAKENHI Grant No. JP26K01411.

DATA AVAILABILITY

The data that support the findings of this article are not publicly available upon publication because it is not technically feasible and/or the cost of preparing, depositing, and hosting the data would be prohibitive within the terms of this research project. The data are available from the authors upon reasonable request.

[1] D. N. Basov, R. D. Averitt, and D. Hsieh, Towards properties on demand in quantum materials, Nat. Mater. **16**, 1077 (2017).
[2] A. Eckardt, *Colloquium*: Atomic quantum gases in periodically driven optical lattices, Rev. Mod. Phys. **89**, 011004 (2017).
[3] M. Bukov, L. D'Alessio, and A. Polkovnikov, Universal high-frequency behavior of periodically driven systems: From dynamical stabilization to Floquet engineering, Adv. Phys. **64**, 139 (2015).
[4] T. Oka and S. Kitamura, Floquet engineering of quantum materials, Annu. Rev. Condens. Matter Phys. **10**, 387 (2019).
[5] U. D. Giovannini and H. Hübener, Floquet analysis of excitations in materials, J. Phys.: Mater. **3**, 012001 (2019).
[6] M. S. Rudner and N. H. Lindner, Band structure engineering and non-equilibrium dynamics in Floquet topological insulators, Nat. Rev. Phys. **2**, 229 (2020).
[7] A. de la Torre, D. M. Kennes, M. Claassen, S. Gerber, J. W. McIver, and M. A. Sentef, *Colloquium*: Nonthermal pathways to ultrafast control in quantum materials, Rev. Mod. Phys. **93**, 041002 (2021).
[8] H. Lignier, C. Sias, D. Ciampini, Y. Singh, A. Zenesini, O. Morsch, and E. Arimondo, Dynamical control of matter-wave tunneling in periodic potentials, Phy. Rev. Lett. **99**, 220403 (2007).
[9] A. Zenesini, H. Lignier, D. Ciampini, O. Morsch, and E. Arimondo, Coherent control of dressed matter waves, Phys. Rev. Lett. **102**, 100403 (2009).
[10] M. Aidelsburger, M. Atala, S. Nascimbène, S. Trotzky, Y.-A. Chen, and I. Bloch, Experimental realization of strong effective magnetic fields in an optical lattice, Phys. Rev. Lett. **107**, 255301 (2011).
[11] C. V. Parker, L.-C. Ha, and C. Chin, Direct observation of effective ferromagnetic domains of cold atoms in a shaken optical lattice, Nat. Phys. **9**, 769 (2013).
[12] G. Jotzu, M. Messer, R. Desbuquois, M. Lebrat, T. Uehlinger, D. Greif, and T. Esslinger, Experimental realization of the topological Haldane model with ultracold fermions, Nature (London) **515**, 237 (2014).
[13] M. Lohse, C. Schweizer, O. Zilberberg, M. Aidelsburger, and I. Bloch, A Thouless quantum pump with ultracold bosonic atoms in an optical superlattice, Nat. Phys. **12**, 350 (2016).
[14] S. Nakajima, T. Tomita, S. Taie, T. Ichinose, H. Ozawa, L. Wang, M. Troyer, and Y. Takahashi, Topological Thouless pumping of ultracold fermions, Nat. Phys. **12**, 296 (2016).
[15] N. Fläschner, B. S. Rem, M. Tarnowski, D. Vogel, D.-S. Lühmann, K. Sengstock, and C. Weitenberg, Experimental reconstruction of the Berry curvature in a Floquet Bloch band, Science **352**, 1091 (2016).
[16] T. Li, L. Duca, M. Reitter, F. Grusdt, E. Demler, M. Endres, M. Schleier-Smith, I. Bloch, and U. Schneider, Bloch state tomography using Wilson lines, Science **352**, 1094 (2016).
[17] T. Oka and H. Aoki, Photovoltaic Hall effect in graphene, Phys. Rev. B **79**, 081406(R) (2009).
[18] T. Kitagawa, T. Oka, A. Brataas, L. Fu, and E. Demler, Transport properties of nonequilibrium systems under the application of light: Photoinduced quantum Hall insulators without Landau levels, Phys. Rev. B **84**, 235108 (2011).
[19] N. H. Lindner, G. Refael, and V. Galitski, Floquet topological insulator in semiconductor quantum wells, Nat. Phys. **7**, 490 (2011).
[20] R. Wang, B. Wang, R. Shen, L. Sheng, and D. Y. Xing, Floquet Weyl semimetal induced by off-resonant light, Europhys. Lett. **105**, 17004 (2014).
[21] S. Ebihara, K. Fukushima, and T. Oka, Chiral pumping effect induced by rotating electric fields, Phys. Rev. B **93**, 155107 (2016).
[22] H. Hübener, M. A. Sentef, U. De Giovannini, A. F. Kemper, and A. Rubio, Creating stable Floquet–Weyl semimetals by laser-driving of 3D Dirac materials, Nat. Commun. **8**, 13940 (2017).
[23] A. Kundu, H. A. Fertig, and B. Seradjeh, Floquet-engineered valleytronics in dirac systems, Phys. Rev. Lett. **116**, 016802 (2016).
[24] D. Shin, H. Hübener, U. De Giovannini, H. Jin, A. Rubio, and N. Park, Phonon-driven spin-Floquet magneto-valleytronics in MoS_2, Nat. Commun. **9**, 638 (2018).
[25] Y. Hirai, S. Okumura, N. Yoshikawa, T. Oka, and R. Shimano, Floquet Weyl states at one-photon resonance: An origin of nonperturbative optical responses in three-dimensional materials, Phys. Rev. Res. **6**, L012027 (2024).
[26] Y. H. Wang, H. Steinberg, P. Jarillo-Herrero, and N. Gedik, Observation of floquet-bloch states on the surface of a topological insulator, Science **342**, 453 (2013).
[27] F. Mahmood, C.-K. Chan, Z. Alpichshev, D. Gardner, Y. Lee, P. A. Lee, and N. Gedik, Selective scattering between Floquet–Bloch and Volkov states in a topological insulator, Nat. Phys. **12**, 306 (2016).
[28] S. Ito *et al.*, Build-up and dephasing of Floquet–Bloch bands on subcycle timescales, Nature (London) **616**, 696 (2023).
[29] S. Zhou *et al.*, Pseudospin-selective Floquet band engineering in black phosphorus, Nature (London) **614**, 75 (2023).
[30] M. Merboldt *et al.*, Observation of Floquet states in graphene, Nat. Phys. **21**, 1093 (2025).
[31] D. Choi, M. Mogi, U. De Giovannini, D. Azoury, B. Lv, Y. Su, H. Hübener, A. Rubio, and N. Gedik, Observation of Floquet–Bloch states in monolayer graphene, Nat. Phys. **21**, 1100 (2025).
[32] Q. T. Vu, H. Haug, O. D. Mücke, T. Tritschler, M. Wegener, G. Khitrova, and H. M. Gibbs, Light-induced gaps in semiconductor band-to-band transitions, Phys. Rev. Lett. **92**, 217403 (2004).

[33] E. J. Sie, C. H. Lui, Y.-H. Lee, L. Fu, J. Kong, and N. Gedik, Large, valley-exclusive Bloch-Siegert shift in monolayer WS_2, Science **355**, 1066 (2017).
[34] J.-Y. Shan, M. Ye, H. Chu, S. Lee, J.-G. Park, L. Balents, and D. Hsieh, Giant modulation of optical nonlinearity by Floquet engineering, Nature (London) **600**, 235 (2021).
[35] Y. Murotani, N. Kanda, T. N. Ikeda, T. Matsuda, M. Goyal, J. Yoshinobu, Y. Kobayashi, S. Stemmer, and R. Matsunaga, Stimulated Rayleigh scattering enhanced by a longitudinal plasma mode in a periodically driven Dirac semimetal Cd_3As_2, Phys. Rev. Lett. **129**, 207402 (2022).
[36] J. W. McIver, B. Schulte, F.-U. Stein, T. Matsuyama, G. Jotzu, G. Meier, and A. Cavalleri, Light-induced anomalous Hall effect in graphene, Nat. Phys. **16**, 38 (2020).
[37] N. Yoshikawa *et al.*, Light-induced anomalous Hall conductivity in the massive three-dimensional Dirac semimetal $Co_3Sn_2S_2$, Phys. Rev. B **111**, 245104 (2025).
[38] P. L. Kapitza, Dynamic stability of the pendulum with vibrating suspension point, Sov. Phys. JETP **21**, 588 (1951).
[39] S. Nakamura, K. Katsumi, H. Terai, and R. Shimano, Nonreciprocal terahertz second-harmonic generation in superconducting NbN under supercurrent injection, Phys. Rev. Lett. **125**, 097004 (2020).
[40] C. Vaswani *et al.*, Terahertz second-harmonic generation from lightwave acceleration of symmetry-breaking nonlinear supercurrents, Phys. Rev. Lett. **124**, 207003 (2020).
[41] Y. Kawakami *et al.*, Petahertz non-linear current in a centrosymmetric organic superconductor, Nat. Commun. **11**, 4138 (2020).
[42] F. Sekiguchi, H. Narita, H. Hirori, T. Ono, and Y. Kanemitsu, Anomalous behavior of critical current in a superconducting film triggered by DC plus terahertz current, Nat. Commun. **15**, 4435 (2024).
[43] J. N. Bardsley and M. J. Comella, ac Stark effect for short-range potentials with intense electromagnetic fields, Phys. Rev. A **39**, 2252 (1989).
[44] J. H. Eberly and K. C. Kulander, Atomic stabilization by superintense lasers, Science **262**, 1229 (1993).
[45] K. Na, D. Jarukanont, and L. E. Reichl, Dynamics of quasibound state formation in the driven Gaussian potential, Phys. Rev. E **77**, 046208 (2008).
[46] O. Neufeld, D. Podolsky, and O. Cohen, Floquet group theory and its application to selection rules in harmonic generation, Nat. Commun. **10**, 405 (2019).
[47] T. V. Trevisan, P. V. Arribi, O. Heinonen, R.-J. Slager, and P. P. Orth, Bicircular light floquet engineering of magnetic symmetry and topology and its application to the dirac semimetal Cd_3As_2, Phys. Rev. Lett. **128**, 066602 (2022).
[48] Y. Ikeda, S. Kitamura, and T. Morimoto, Photocurrent induced by a bicircular light drive in centrosymmetric systems, Phys. Rev. Lett. **131**, 096301 (2023).
[49] I. Tyulnev, Á. Jiménez-Galán, J. Poborska, L. Vamos, P. St. J. Russell, F. Tani, O. Smirnova, M. Ivanov, R. E. F. Silva, and J. Biegert, Valleytronics in bulk MoS_2 with a topologic optical field, Nature (London) **628**, 746 (2024).
[50] S. Mitra, Á. Jiménez-Galán, M. Aulich, M. Neuhaus, R. E. F. Silva, V. Pervak, M. F. Kling, and S. Biswas, Lightwave-controlled Haldane model in monolayer hexagonal boron nitride, Nature (London) **628**, 752 (2024).
[51] E. Timurdogan, C. V. Poulton, M. J. Byrd, and M. R. Watts, Electric field-induced second-order nonlinear optical effects in silicon waveguides, Nat. Photon. **11**, 200 (2017).
[52] D. J. Cook, J. X. Chen, E. A. Morlino, and R. M. Hochstrasser, Terahertz-field-induced second-harmonic generation measurements of liquid dynamics, Chem. Phys. Lett. **309**, 221 (1999).
[53] O. A. Aktsipetrov *et al.*, dc-electric-field-induced and low-frequency electromodulation second-harmonic generation spectroscopy of Si (001)–SiO_2 interfaces, Phys. Rev. B **60**, 8924 (1999).